



Recrystallization behavior and thermal shock resistance of the W-1.0 wt% TaC alloy

Z.M. Xie^a, S. Miao^a, T. Zhang^{a,*}, R. Liu^a, X.P. Wang^a, Q.F. Fang^{a,**}, T. Hao^a, Z. Zhuang^a, C.S. Liu^a, Y.Y. Lian^b, X. Liu^b, L.H. Cai^c

^a Key Laboratory of Materials Physics, Institute of Solid State Physics, Chinese Academy of Sciences, Hefei, Anhui 230031, China

^b Southwestern Institute of Physics, Chengdu, Sichuan 610041, China

^c ATTL Advanced Materials Co., Ltd, Beijing 100083, China

ARTICLE INFO

Article history:

Received 13 October 2017

Received in revised form

19 January 2018

Accepted 22 January 2018

Available online 2 February 2018

Keywords:

Tungsten

TaC

Recrystallization

Mechanical properties

Thermal shock resistance

ABSTRACT

The high-temperature stability and good mechanical strength of tungsten (W) alloys are highly desirable for a wide range of fusion applications, which can be achieved by dispersion strengthening. In this paper, TaC dispersion effects on the thermal stabilities, tensile properties and thermal shock resistances have been investigated. A hot-rolled W-1.0 wt% TaC plate has been fabricated which contains the high tensile strength and elongation. Nanosized particles in the W matrix improve the recrystallization temperature to about 1400 °C and the ultimate tensile strength to 571 MPa at 500 °C through hindering grain boundary migration, pinning dislocations and refining grains. The effects of edge-localized mode like transient heat events on the rolled and recrystallized W-1.0 wt% TaC alloys were investigated systematically. The cracking threshold (100 shots) at room temperature is in the range of 0.33–0.44 GW/m² for the rolled W-1.0 wt% TaC. Recrystallization degrades mechanical strength and makes the material more prone to thermal shock damages. Coarse Ta₂O₅ and Ta-C_x-O_y particles are easy to fracture and introduce a preferential crack initiation in W matrix during cyclic heat loads.

© 2018 Elsevier B.V. All rights reserved.

1. Introduction

Tungsten (W) is a refractory metal that keeps its body-centered cubic (bcc) crystal structure from room temperature (RT) all the way to its high melting temperature of 3410 °C. W materials offer excellent high-temperature strength, high neutron load capacity and high thermal conductivity [1–3]. Thus it has attracted growing interest as plasma facing materials in future fusion reactors. However, inherent disadvantages of pure tungsten materials are always serious issues for the fusion reactor applications. These issues include the poor low-temperature machinability, high ductile-brittle transition temperature (DBTT = 150–600 °C) and irradiation induced embrittlement [4–6], which are directly correlated to materials ductility and grain boundary (GB) strength [7]. In fusion reactors, high service temperatures for divertor target components (~1200 °C) [8] can alter the microstructures by recovery,

recrystallization and grain growth [9], which degrade mechanical strength and lead to severe embrittlement [10–12]. Therefore, W alloys with steady thermal and mechanical properties at elevated temperatures are highly desirable for high-temperature applications.

It has been indicated that brittle fractures in W mainly occur along grain boundaries (GBs) due to the impurity (e.g., N, and O) segregation at the GBs and the weakness of GBs with random orientations [13,14]. In this sense, approaches with modifying impurity distribution on GBs would improve the strength and ductility. For example, minor alloying elements such as Zr can be used to purify the GBs by reacting with O to form second phase particles ZrO_x, which could diminish the influence of O elements on GBs [15]. Nanosized carbides, such as tantalum carbide (TaC), also have the same ability of capturing free O to purify GBs [16]. In addition, TaC with a relatively higher melting temperature (3880 °C) and good thermal stability can enhance the erosion resistance of W-TaC materials [17]. These superior performances make TaC very attractive in fabricating W based composites: the dispersion of nano sized TaC is effective in enhancing the mechanical strength.

In future fusion devices such as ITER, plasma facing materials

* Corresponding author.

** Corresponding author.

E-mail addresses: zhangtao@issp.ac.cn (T. Zhang), qffang@issp.ac.cn (Q.F. Fang).

will be exposed to steady-state heat loads with a power density of 5–20 MW/m² in the divertor area and transient events such as edge localized modes, disruptions and vertical displacement events with heat loads up to several GW/m² [18–20]. High temperatures and high thermal stresses developed during transients could lead to the surface modification, crack formation, recrystallization and melting. These material damages can limit the power-handling capacity of plasma facing components, decrease the lifetime and lead to plasma contaminations. For W-TaC materials, thermal stabilities and thermal shock responses are much less reported than that of pure W [21–23]. Nano oxide or carbide dispersion strengthened W materials commonly shown a significant increase in recrystallization temperature because these dispersed particles can pin GBs to hinder grain growth [24]. While the crack formation mechanism for carbide dispersion strengthened W (CDS-W) under the thermal loads still remains a scientific ambiguity, especially in the recrystallization stage. Generally, particle size, distribution of dispersoids and detrimental impurities would strongly affect the thermal shock resistance of CDS-W [25–27]. Such microstructural discrepancy between CDS-W and pure W may generate different mechanisms for cracking formation during high thermal loads, which should be thoroughly studied and fully understood.

In this paper, the recrystallization behavior of the rolled W-1.0 wt% TaC was investigated by isochronal annealing in a temperature range from 1200 °C to 1700 °C. In order to explore the influences of dispersed particles on the thermal shock response as well as the mechanical properties, the as rolled and full recrystallized W-1.0 wt% TaC (hereafter abbreviated as WTAC and RWTAC, respectively) samples were exposed to cyclic thermal shocks on an electron beam facility (EMS-60) at South Western Institute of Physics, China. Besides, metallographic analysis, Vickers micro-hardness tests, tensile tests and microstructure analysis were employed to investigate effects of dispersed particles on mechanical properties, thermal stabilities and thermal shock resistances.

2. Methods

2.1. Materials fabrication

WTAC samples were fabricated using pure W powders with particle size of sub-micrometer (purity > 99.9% trace metals basis) and nano-sized TaC powders (average particle size of 80 nm, purity > 99%). The detailed chemical compositions of the as received W and TaC powders (wt.%) were tested and shown in Table 1. A horizontal planetary ball milling machine (WXQM-4B, purchased from the Tencan powder technology co., LTD.) was used. The mixed powders were milled in four WC/Co vessels (having an inside

volume of 10⁻³ m³) together with WC/Co balls (8 mm in diameter) for 10 h in argon atmosphere (oxygen < 0.1 ppm, H₂O < 0.1 ppm) with ball to powder weight ratio of 8:1 and a rotation speed of 350 rpm. WC/Co balls and vessels were used to minimize the possible impurity contamination. The mixed powders were subsequently sintered at 1900 °C at a unidirectional pressure of 30 MPa for 12 h in vacuum (~5E-5 mbar). The sintered blank has a density of ~17.5 g/cm³, corresponding to a relative density of ~91% as shown in Table 2. Then the sintered blank was hot-rolled into a plate with the width of about 110 mm, the length of about 380 mm and the thickness of 4.0 mm (with a total 90% thickness reduction through six-step thermomechanical treatment with each step deformation of 15%, 20%, 35%, 35%, 40% and 40%, respectively, at 1600 °C). Rolling processes can effectively eliminate the porosity by plastic deformation and thus achieve a nearly full density as shown in comparison results in Table 2. After the multistep rolling, the density of this rolled plate reaches up to 19.1 g/cm³, corresponding to a relative density of ~99.6%. The consolidation and rolling were done by collaborating with Beijing Tianlong Tungsten & Molybdenum Co., Ltd. After these multistep fabrication routes including ball milling, sintering and rolling, the gaseous impurity especially the oxygen as well as the cobalt (Co) contents in the WTAC were to some extent increased as shown in Table 1. The Co contamination may come from WC/Co balls and vessels during the high energy ball milling. After the following annealing, there is a little change (of these contamination contents) in the RWTAC compared to the WTAC as shown in Table 1. In this work, the full recrystallized W-1.0 wt% TaC (RWTAC) sample was annealed at 1600 °C for 1 h in vacuum (~5E-5 mbar).

2.2. Mechanical properties tests

For tensile tests, the dog-bone-shaped samples with a cross-section of 1.5 × 0.75 mm² and a working length of 5 mm along rolling direction (RD) were cut by a Wire cut Electrical Discharge Machining (WEDM). The tensile direction of all tested samples is parallel to the RD. These specimens were polished with 2000 mesh SiC papers before tests. All tensile samples were tested using an Instron-5967 machine at a constant speed of 0.06 mm/min (corresponding to a nominal strain rate of 2 × 10⁻⁴) in air. The total elongation is defined as the strain to fracture in accordance with the standard ASTM E8M. For tensile tests, three to five samples were tested at each temperature ranging from 100 to 500 °C to ensure repeatability. Before Vickers micro-hardness tests, specimens were electrolytically polished in 2% sodium hydroxide aqueous solution at RT with a polishing voltage of 18 V and a current density about 3 mA/mm², to obtain the mirror-polished and

Table 1
Chemical composition of as received W powders, TaC powders, WTAC and RWTAC (wt. ppm).

	Nb	Mo	Fe	O	C	Ar	N	Co	W	Ta
W Powder	<0.01	20	0.5	718	64	<0.01	109	<0.1	Bal	5.1
TaC Powder	15	0.01	<0.01	3200	6.3E4	<0.01	403	<0.1	<0.01	Bal
WTAC	<0.01	20	0.5	1450	660	<0.01	358	4.7	Bal	9480
RWTAC	<0.01	19	0.5	1570	729	<0.01	405	4.3	Bal	9250

Table 2
Summary of room-temperature properties of the W-1.0 wt% TaC alloy.

Materials	Density (g/cm ³)	Relative density (%)	Vickers microhardness (HV)	DBTT (°C)
As sintered W-1.0% TaC	17.5 ± 0.04	91.2 ± 0.2	316	—
WTAC	19.1 ± 0.04	99.6 ± 0.2	486	~200
RWTAC	19.1 ± 0.04	99.6 ± 0.2	410	~200

stress-free surfaces. Vickers microhardness tests were conducted with a load of 200 N and a constant indenter dwell time of 30 s. After indentation, the length of the two diagonals of the square-shaped Vickers indentation was immediately measured by optical microscopy with a magnification of 300 with an error of measurement of $\pm 1 \mu\text{m}$. The thermal stability of WTAC samples was evaluated by isothermal annealing in a temperature range between 1300 °C and 1600 °C for an annealing time up to 50 h. In addition, Vickers microhardness measurements were performed to track softening related to recovery and recrystallization by isochronal annealing for 1 h in a temperature range from 1200 °C to 1700 °C.

2.3. Microstructure characterization

The microstructure was characterized by Transmission electron microscope (TEM, JEM-2000FX). TEM samples were prepared by twin-jet in Tenuple-5 (reagents: 2 wt% NaOH aqueous solution). The metallography was obtained using an optical microscope (ZEISS-AX10) after polishing and etching (10% potassium ferricyanide with 10% sodium hydroxide aqueous solution). The volume fraction of both intergranular (and intragranular) particles and average particle size have been statistically analyzed using quantitative metallography in accordance with ASTM standard E112-10. The thermal loaded surfaces and cross-sections of samples were characterized by field emission scanning electron microscopy (FESEM, SU8020 Hitachi).

2.4. Thermal shock tests

In order to investigate the influence of recrystallization on the thermal shock damage response of WTAC, thermal shock tests were performed along with normal direction (ND) of the rolled and recrystallized W-TaC alloys using the electron beam device EMS-60 (60 kW Electron-beam Material-test Scenario). The acceleration voltage and maximum electron current of this electron beam were in the range of 90–150 kV and 400 mA, respectively. The pulse duration was from 1 ms to continuous operation and the beam rise time was less than 0.3 ms [28,29]. In this experiment, a Gaussian shaped electron beam with a focused diameter of approximately 1 mm (FWHM) and an acceleration voltage of 120 kV was used. The used absorption coefficient for tungsten was ~ 0.55 , which corresponded to the value obtained by means of Monte-Carlo simulations [22], and was in agreement with the reported experimental data [29]. It's worth noting that the directly detected absorption coefficient for the present W-TaC alloy was about 0.46 in the absorbed current measurement. With further considering the process of the emission of secondary and thermionic electrons which also contributed to the heat but not to the current through the sample [30], the finally used absorption coefficient for W-TaC alloys was ~ 0.55 . The exposed area ($4 \text{ mm} \times 4 \text{ mm}$) was scanned with a fast scanning frequencies (37 kHz in x-direction and 27 kHz in y-direction, respectively) on specimens with the specimen size of $10 \times 10 \times 4 \text{ mm}^3$. These specimens were placed on a water-cooled copper substrate. All tests were performed with a total number of 100 pulses with the pulse duration of 1 ms and the inter-pulse time was 5 s to allow a complete cool down to RT. In this study, four different absorbed power densities (APD, 0.22, 0.33, 0.44 and 0.55 GW/m^2) were selected to investigate the thermal shock damage response of the as-rolled and recrystallized WTAC alloys.

3. Results and discussion

3.1. Recrystallization of the rolled WTAC

Metallographic analysis and Vickers microhardness were used

to determine the recrystallization temperature of WTAC. Metallographic micrographs of WTAC samples exhibit elongated grains with an average length of $41.7 \mu\text{m}$ along the RD and a length-width ratio of 4/1 as shown in Fig. 1a. When the annealing temperature was up to 1400 °C, tungsten grains still shown the elongated shape with the average length of $46.3 \mu\text{m}$ but an increasing length-width ratio of about 3/1, indicating the occurrence of recrystallization and grain growth as shown in Fig. 1b. The average length and aspect ratio of tungsten grains further changed to $71.2 \mu\text{m}$ and 2.5/1, respectively, with increasing the annealing temperature to 1450 °C as shown in Fig. 1c. After 1500 °C annealing for 1 h, some grains grown into equiaxed structures as shown in Fig. 1d. Further increasing annealing temperature to 1600 °C, almost all grains recrystallized and grown into coarse grains (resulting in an average length of $132.6 \mu\text{m}$ in RD and an average width of $83.2 \mu\text{m}$ in ND, respectively) as shown in Fig. 1e, suggesting the full recrystallization. Defining the recrystallization temperature as the starting temperature at which deformed materials undergo a change of grain size/aspect ratio, here the recrystallization temperature of the WTAC alloys is 1400 °C.

It is well known that the micro-hardness is closely related to the microstructure, therefore the recrystallization behavior could be confirmed by the evolution of hardness with the annealing temperature [31,32]. The micro-hardness of WTAC samples is 486 HV, about $\sim 50 \text{ HV}$ higher than that of the rolled pure W [33]. The referred rolled pure W has the similar thickness reduction ($\sim 90\%$) and the elongated grain shape with a length-width ratio of 4/1 but larger grain size ($\sim 200 \mu\text{m}$ in length and $50 \mu\text{m}$ in width). The different grain size and dispersed TaC particles between the present WTAC and reported pure W lead to the different hardness: the larger grain size resulting in the relatively lower hardness in the rolled pure W. After annealing at 1200 °C, 1300 °C and 1400 °C for 1 h, the Vickers microhardness of annealed WTAC specimens are 472, 470 and 468 HV, respectively, about 3.7% lower than that of the as-rolled one as shown in Fig. 1f. A rapid hardness decrease occurs after annealing at the higher annealing temperatures ($> 1400 \text{ °C}$). For example, the hardness decreased to 464 HV and 446 HV after annealing at 1450 °C and 1500 °C for 1 h, respectively, which came from the recrystallization and grain growth. After the full recrystallization at 1600 °C, the hardness reaches a minimum value of about 410 HV and keeps constant with further increasing the annealing temperature to 1700 °C. This Vickers microhardness evolution with the annealing temperature further confirms the recrystallization process (the starting recrystallization temperature between 1400 and 1500 °C) as indicated by the above metallographic analysis. Based on the combination of metallographic images and hardness evaluation, the recrystallization temperature of WTAC can be considered as 1400 °C, about 200 °C higher than that of rolled pure W with the similar thickness reduction [33]. This increased recrystallization temperature is mainly attributed to the nanosized dispersoids hindering GB migration at elevated temperatures.

The evolutions of Vickers micro-hardness with annealing time at two different temperatures are presented in Fig. 2. A monotonous decrease in hardness is observed from the value $\text{HV}_{\text{def}} = 485 \pm 2 \text{ HV}$ of an as-rolled state to the value $\text{HV}_{\text{rex}} = 407 \pm 4 \text{ HV}$ of a fully recrystallized state. Two different softening stages can be distinguished in Fig. 2. The first one corresponds to an initial decrease of hardness and slows down over the time, which is caused by dislocation recovery processes (as schematically illustrated by the dashed line in Fig. 2b). The second stage occurs at longer annealing times and entails a higher reduction in hardness, which is caused by recrystallization (the solid line in Fig. 2b).

A signal of the loss in hardness during annealing can be characterized by the time $t_{\Delta\text{HV}/2}$ required to attain the hardness

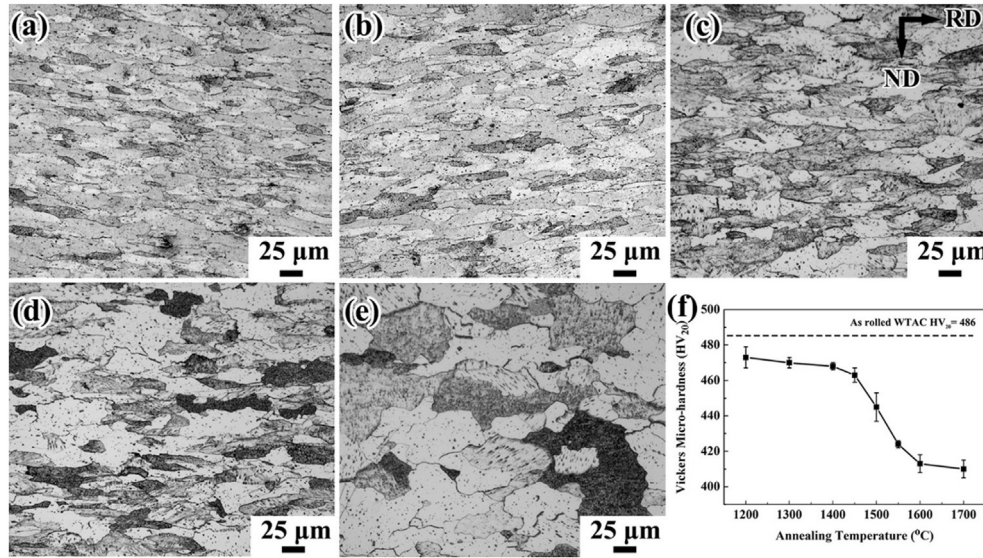


Fig. 1. Optical micrographs and Vickers microhardness of the WTAC after annealing for 1 h at various temperatures: (a) as-rolled samples, (b) annealed at 1400 °C, (c) annealed at 1450 °C, (d) annealed at 1500 °C, (e) annealed at 1600 °C and (f) the evolution of Vickers microhardness with annealing temperatures.

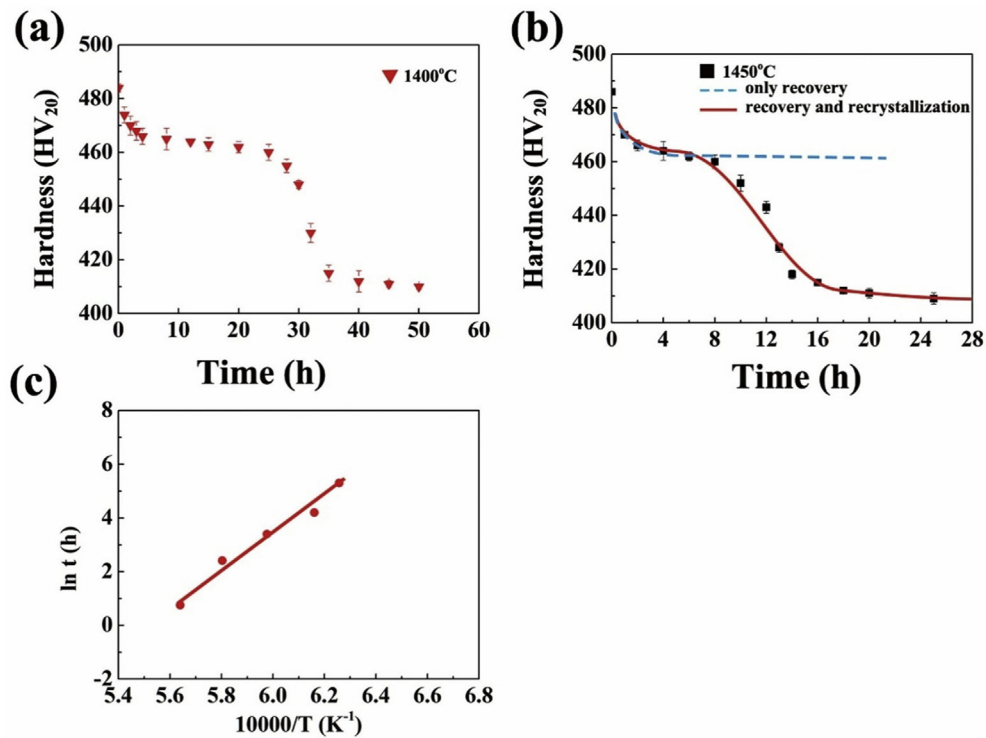


Fig. 2. Evolution of the Vickers microhardness of the WTAC with annealing time (a) at 1400 °C, (b) 1450 °C and (c) Arrhenius plot of the annealing time at half of the total hardness loss of WTAC versus the reciprocal of the annealing temperature.

$(HV_{\text{def}} + HV_{\text{rex}})/2 = 447$ HV, i.e. when half hardness loss has occurred. The annealing time to reach half hardness loss are estimated by linear interpolation from Fig. 2c. The dependence of the time to half hardness loss on annealing temperature follows closely an Arrhenius relation [9].

$$t_{\Delta HV/2} = t_{\Delta HV/2}^* \exp\left(\frac{E_{\Delta HV/2}}{RT}\right) \quad (1)$$

where $t_{\Delta HV/2}^*$ is a pre-factor, R is the universal gas constant and

$E_{\Delta HV/2}$ is the apparent recrystallization activation energy. From the Arrhenius plot shown in Fig. 2c the $E_{\Delta HV/2}$ can be estimated by linear fitting as 478 kJ/mol, which is higher than the value of 357 kJ/mol obtained in a previous study on similarly deformed W [33]. It's well known that the recrystallization is a thermally activated process related to the interface migration [34]. The activation energy for boundary migration (the activation energy for recrystallization) depends on several parameters including the boundary structure which, in a given material, is a function of misorientation and boundary plane. It is also strongly influenced by defects in the

material such as point defects and second phase particles. In the WTAC, the higher activation energy for recrystallization could be attributed to nanosized TaC particles (average: ~83 nm) to keep grain structures stable. From equation (1) the incubation time for recrystallization can be extrapolated by using the obtained activation energy. Accordingly, a lifespan of about 4.4 months at service temperature of 1200 °C can be calculated for the WTAC.

3.2. Tensile properties before/after recrystallization

The tensile engineering stress-strain curves are presented in Fig. 3. The WTAC (Fig. 3a) shown typical brittle fractures at 100 °C and turned into plasticity at 200 °C with an average ultimate tensile strength (UTS) of 864 MPa and an average total elongation (TE) of ~9.6%. Defining the DBTT as the lowest temperature at which a sample undergoes a minimum elongation >5% without failure, here the DBTT of the WTAC is about 200 °C, which is equal to the recently reported rolled pure W [35], swaged W-0.5HfC alloy [36], and about 100 °C higher than that of the rolled W-0.5ZrC alloy [24]. In order to clearly present the tensile properties, the ultimate tensile strength (UTS), yield stress (YS, 0.2% proof stress), uniform elongation (UE) and total elongation (TE) against the test temperatures are shown in Fig. 4, where the result of the as rolled pure W [35], as rolled (WZrC)/recrystallized (RWZrC) W-0.5ZrC alloys [24] and as swaged W-0.5HfC (WHfC) alloy [36] are also presented for comparison. It's can be seen that the UTS of the WTAC is similar to the swaged WHfC, slightly lower than that of the WZrC and about 200 MPa higher than that of the rolled pure W as shown in Fig. 4a. For the TE, the WTAC has the similar TE values to that of the WHfC and WZrC

alloys, but these TE values (about 15%, at 300, 400 and 500 °C) are just a half of the rolled pure W as shown in Fig. 4b. It's interesting to note that the TE of WTAC at 200 °C is about 11%, which is the highest one compared to the as rolled pure W (2.5%), as swaged WHfC (0.4%) and the WZrC (6.8%). To sum up, the dispersion strengthened microstructures in WTAC could improve the strength but to some extent decrease the tensile elongation.

After the full recrystallization, the RWTAC (Fig. 3b) still shown typical brittle fractures at 100 °C and turned into plasticity at 200 °C with an average ultimate tensile strength (UTS) of 560 MPa and an average total elongation (TE) of ~16.8%. That's to say, the recrystallization and grain growth did not increase the DBTT of the rolled W-1.0 wt% TaC alloy. Intuitively, the UTS of the RWTAC decreases obviously (about 320 MPa lower than that of the WTAC), which can be attributed to dislocation elimination and grain growth [37,38]. The RWTAC, however, exhibits obvious work hardening instead of necking, which is reflected in the markedly increased uniform elongation as shown in Fig. 4b. For example, the UE of the RWTAC increased from 0.6% (WTAC, at 400 °C or 500 °C) to 35%. In addition, the TE of RWTAC is as high as 55% at 500 °C, about 2.5 times that of the as-rolled one (WTAC) and 1.7 times that of the rolled pure W. Moreover, the RWTAC also exhibits more obvious low-temperature ductility (with a TE of 18% at 200 °C) than that of the rolled pure W (just 2.5%) [35].

As well known, the mechanical and thermal properties are determined by the microstructure of materials. The cross-section micrographs after tensile tests are shown in Fig. 5. Intuitively, transgranular fractured grains in WTAC samples (Fig. 5a) can be clearly observed after tensile tests at 100 °C. Tensile fracture surfaces of as-rolled ones, tested at 300 °C (see Fig. 5b), reveal obvious delamination structures caused by tensile deformation. It's known that high deformation induced by the multistep rolling could introduce the high density of defects like dislocations in the WTAC as shown in the following TEM images (Fig. 6). Moreover, a large number of dislocations tended to pile up at the elongated GBs in the WTAC as shown in Fig. 6a, which would introduce stress concentrations, necking and the possible sites of crack initiation. This explains well the tensile behavior: WTAC samples have fine grains and hence a high yield strength, but neck immediately after yielding (see Fig. 3). In the case of the RWTAC samples, intergranular rupture and equiaxed large grains appear after tensile tests at 100 °C as shown in Fig. 5c. Full recrystallization and grain growth could annihilate dislocations, eliminate sub-grain structures and form new strain-free grains. Moreover, during the recrystallization and/or grain growth a migrating GB can also be saturated by

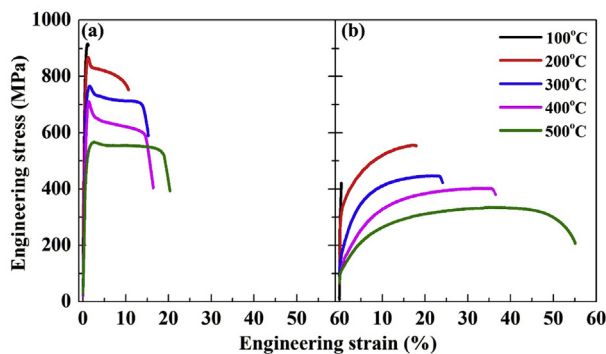


Fig. 3. Tensile behaviors of (a) the WTAC and (b) RWTAC samples.

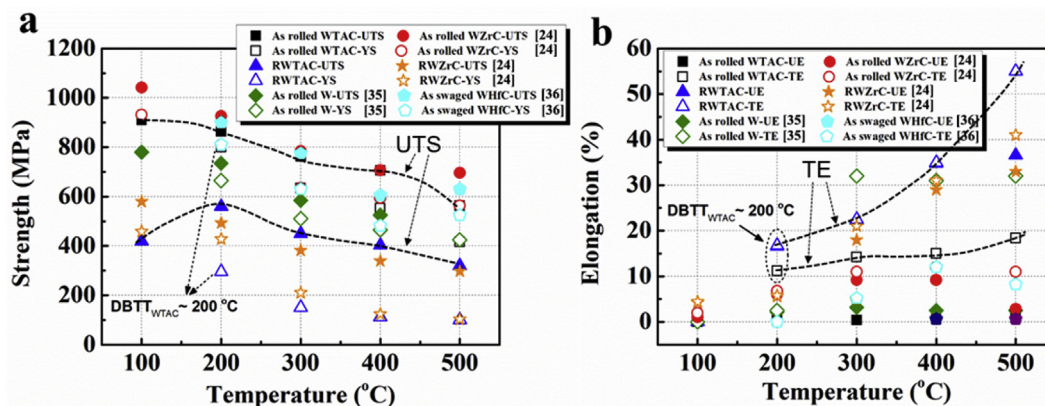


Fig. 4. (a) The tensile yield stress (YS, 0.2% proof stress) and ultimate tensile strength (UTS) and (b) the uniform elongation (UE) and total elongation (TE) against testing temperatures.

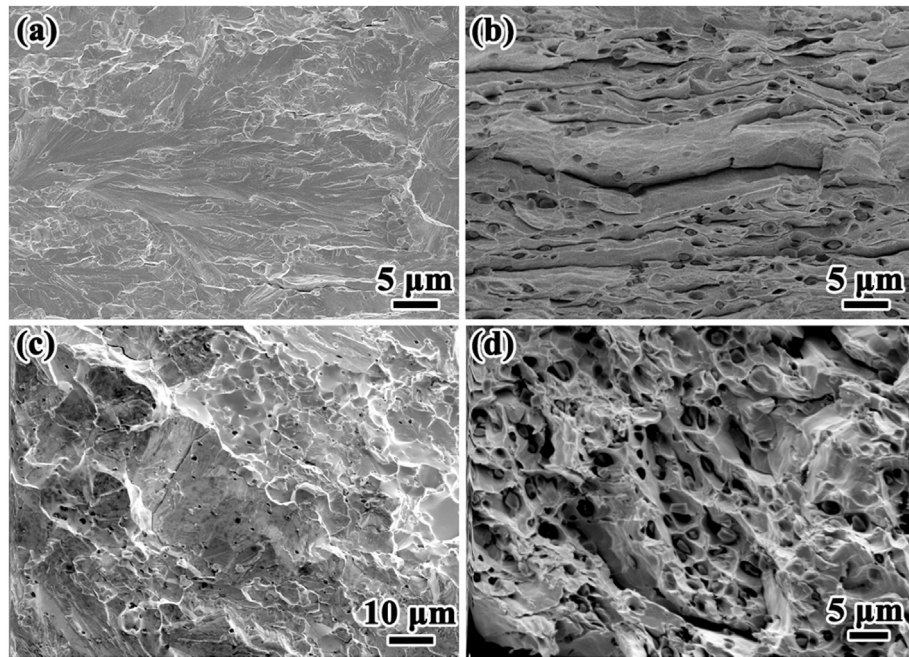


Fig. 5. SEM images of tensile fracture surfaces of WTAC and RWATC: (a) fracture surfaces of WTAC tested at 100 °C, (b) WTAC tested at 300 °C, (c) fracture surfaces of RWATC samples tested at 100 °C and (d) RWATC tested at 300 °C.

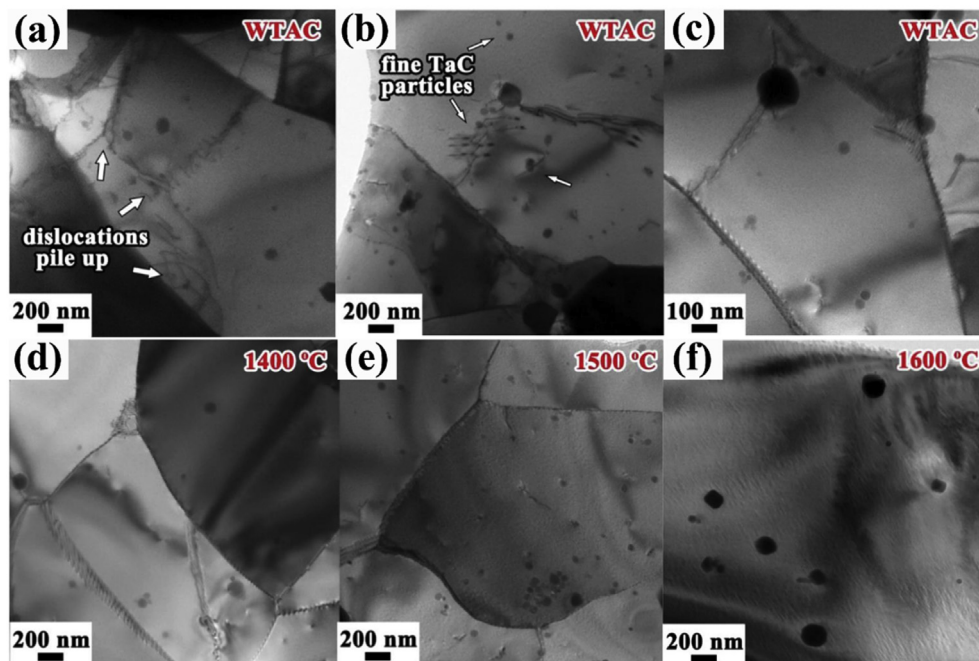


Fig. 6. Typical bright field TEM images showing the microstructures of (a) high concentration of defects generated by hot rolling in WTAC, (b) dislocations interacting with intragranular nano particles in WTAC, (c) nano particles tightly bound to the GBs in WTAC (d) annihilation of dislocations after 1400 °C annealing for 1 h, (e) sub-grain formation after 1500 °C annealing for 1 h and (f) recrystallization and grain growth after 1600 °C annealing for 1 h.

collecting impurities such as the oxygen while sweeping the volume [39,40]. Oxygen impurity is known to give a detrimental effect of decreasing the grain boundary strength of W [39], thus resulting in the low temperature intergranular failure at those grains that have been formed by recrystallization (recrystallization embrittlement). Ductile fractures of RWATC samples after tensile tests at 300 °C illustrate a lot of dimples and reduced delamination areas as shown in Fig. 5d. The tensile fracture surfaces of RWATC imply that

elongated grains are replaced by large equiaxed grains after full recrystallization and grain growth. On the one hand, these newly developed equiaxed grains may be embrittled by the segregation of certain impurity atoms to the GBs, resulting in reduced GB strength. On the other hand, these equiaxed grains are large and almost free of dislocations due to the recrystallization annealing as shown in Fig. 6f. The increased crystal size together with the decreased dislocation density resulted in a low strength of crystals (grains).

Thus these equiaxed grains underwent tensile deformation (forming dimples) rather than direct intergranular fractures during tensile loading at intermediate temperatures. In addition, the strain-free equiaxed grains could provide more rooms to accommodate moving dislocations during the subsequent tensile tests. So the RWATC shows the better tensile plasticity compared to the WTAC. This increase in the tensile plasticity after full recrystallization has also been found in the recently reported rolled W-0.5 wt% ZrC alloy [24].

Further TEM analysis gives more detailed information on microstructures as shown in Fig. 6. Fine W sub-grains and nano-scaled second phase particles have been achieved by strictly controlling the ball milling process, hot-rolling temperature and the amount of deformation. The microstructure evolution with the annealing temperatures is shown in Fig. 6. For WTAC, nanoparticles are uniformly dispersed in tungsten grain interior or located at GBs as shown in Fig. 6a–c. These nanoparticles could pin down (see Fig. 6a and b) and thus accumulate dislocations within grains during the deformation process. Pinned and accumulated dislocations effectively raise strength of WTAC. Meanwhile, nano particles located at GBs (see Fig. 6c) could decrease GB mobility, reduce grain growth rate and thus refine sub-grain structures, which can undoubtedly improve the strength and recrystallization temperature of WTAC. These results emphasize that dispersion strengthened structures can react with dislocations and grain boundaries, resulting in grain mobility inhibition and hence increasing the thermal activation energy for recrystallization. After annealing at 1400 °C (see Fig. 6d), dislocation annihilation and rearrangement occurred in the tungsten interior and resulted in lower energy dislocation configurations. More regular dislocation networks or low angle GBs were eliminated and parts of newly recrystallized tungsten grains formed after 1500 °C annealing (see Fig. 6e). After full recrystallization, reduced defect density and rapid grain growth are found as depicted in Fig. 6f.

The evolutions of the second phase particle distribution with annealing temperatures were also investigated as shown in Fig. 7. The particle size and fraction of both intergranular (and intra-granular) particles were statistically analyzed using quantitative metallography based on about 200 particles in TEM images. In these W-1.0 wt% TaC alloys, there are mainly two categories of dispersoids: most of them are TaC particles with relatively small particle size (~94%, as the statistical results in the red bar chart in Fig. 7) and the other small number of them are Ta₂O₅ (or Ta-C-O) particles with larger particle size (~6%, as the statistical results in the blue bar chart in Fig. 7). The formation of the Ta₂O₅ (or Ta-C-O) has been reported in the previous W-0.5 wt% TaC alloy [16]. In the WTAC, TaC particles have the size range from 25 to 350 nm with an average value of 83 nm and Ta₂O₅ particles have the size range from 260 to 450 nm with an average value of 375 nm as shown in Fig. 7a. After annealing at 1400 °C for 1 h, both the size and fraction of TaC and Ta₂O₅ particles varied negligibly as shown in Fig. 7b. Further increasing the annealing temperature to 1500 °C, the average particle size of TaC and Ta₂O₅ particles increased slightly to 98 nm and 404 nm, respectively, as shown in Fig. 7c. While in the fully recrystallized samples (RWATC), significant increases in the particle sizes of both the TaC and Ta₂O₅ occurred, resulting in the average particle sizes of 126 nm and 545 nm, respectively, as shown in Fig. 7d. In addition, some coarsened Ta₂O₅ particles even have the size larger than 700 nm. That's to say, full recrystallization and grain growth resulted in not only the equiaxed large grains but also the coarsened second particles.

3.3. Thermal shock resistance before/after recrystallization treatments

As a plasma facing material, the thermal shock resistance is a very important property which is closely related to the ductility and strength of tungsten materials [21,41,42]. Usually, the crack

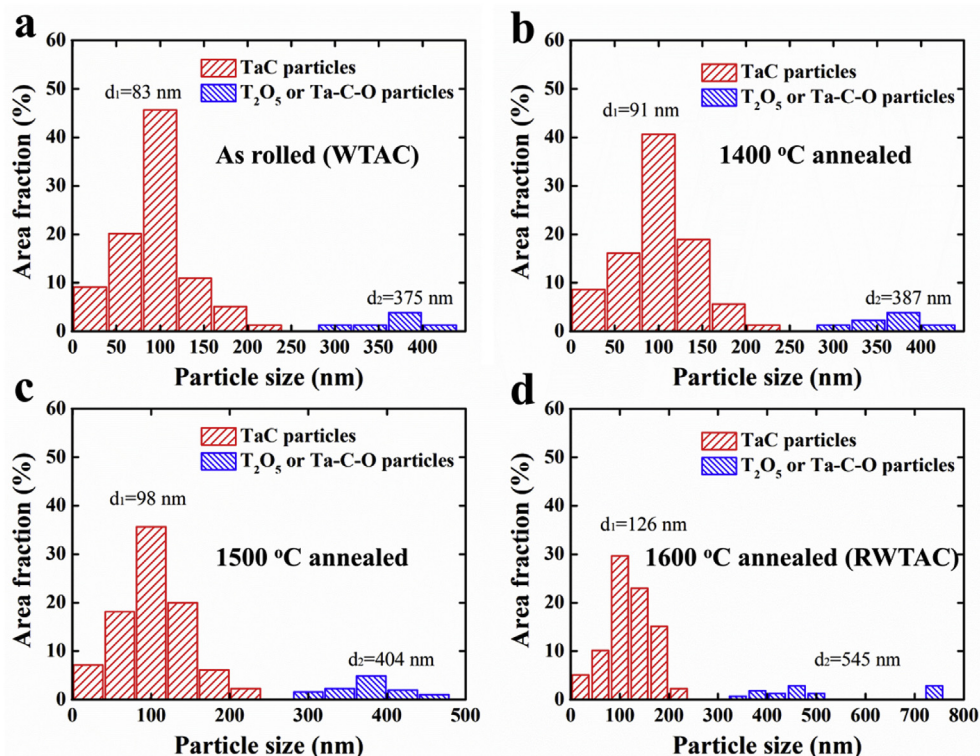


Fig. 7. The statistical results showing the corresponding particle size distribution in the (a) as rolled, (b) 1400 °C/1 h, (c) 1500 °C/1 h and (d) 1600 °C/1 h annealed WTAC alloys.

formation under pulse electron beam loading can be mainly attributed to thermal stresses induced by temperature gradients during the thermal shock tests because the expansion of the volume beneath the heat loaded area was constrained by the cold and rigid bulk material [43]. When the tensile stress generated during the cooling stage is larger than the UTS of materials, cracks will form. Intuitively, if the strength of tungsten materials is high, the crack would be difficultly initiated [41,42]. On the other hand, if there is good ductility, plastic deformation would be easily initiated when thermal stress is larger than the yield strength of the bulk materials, which will relax the thermal stress and thereby prohibit the crack formation in surface and interior.

In order to investigate the effect of dispersion on the thermal shock resistance of WTAC materials, thermal shock tests were conducted upon as-rolled and recrystallized samples at the absorbed power density (APD) ranging from 0.22 to 0.55 GW/m². Fig. 8 shows the loaded surfaces (top views) and cross sectional views (Fig. 8e and i) of WTAC and RWTAC after repetitive (100 pulses) heat loads at RT. An overview result of the thermal shock induced damage for all tested samples is depicted in Fig. 8a. After heat loads (100 pulses, APD ~0.22 GW/m²), no damages were observed in both the WTAC, partially recrystallized WTAC (1500 °C annealed) and the RWTAC (fully recrystallized) samples. Under the heat loads of 0.33 GW/m² with 100 pulses at RT, WTAC samples still shown no surface damages even at a high magnification observation as shown

in Fig. 8b, while small cracks were observed in both the partially and fully recrystallized (RWTAC) samples as shown in Fig. 8f. Several small straight cracks are observed after 100 pulses at 0.44 GW/m² in the WTAC sample surface as shown in Fig. 8c. To sum up, the cracking thresholds at RT are in the range of 0.22–0.33 GW/m² for RWTAC and 0.33–0.44 GW/m² for the WTAC, respectively. These threshold values are larger than that of the reported forged W-UHP (~0.2 GW/m² at RT) [21], which suggest these dispersion strengthened W-TaC alloys have better thermal shock resistances than that of pure W materials. Since the cracking threshold was indicated to be related to the basing temperatures (below or above the material's DBTT) in the thermal shock tests [21,31], all the thermal shock loads were conducted at RT which was below the DBTTs for the WTAC and RWTAC (all about 200 °C). Thus these different threshold values between the WTAC and RWTAC could be related to the different mechanical strength: the higher strength the better thermal shock resistance (in the WTAC). When increasing the APD up to 0.55 GW/m², transgranular cracks grown perpendicular to loaded surfaces (the RD-TD surface) into the material at a certain depth and then extended parallel to the loaded surface as shown in Fig. 8d and e. From Fig. 8e, it can be seen that the cracking depth is about 790 μm for the WTAC after 100 shots with the APD of 0.55 GW/m². This cracking depth (~790 μm) in the WTAC is larger than that of the reported WZrC (~230 μm, 100 shots with the APD of 0.33 GW/m²) [24]. In the case of RWTAC,

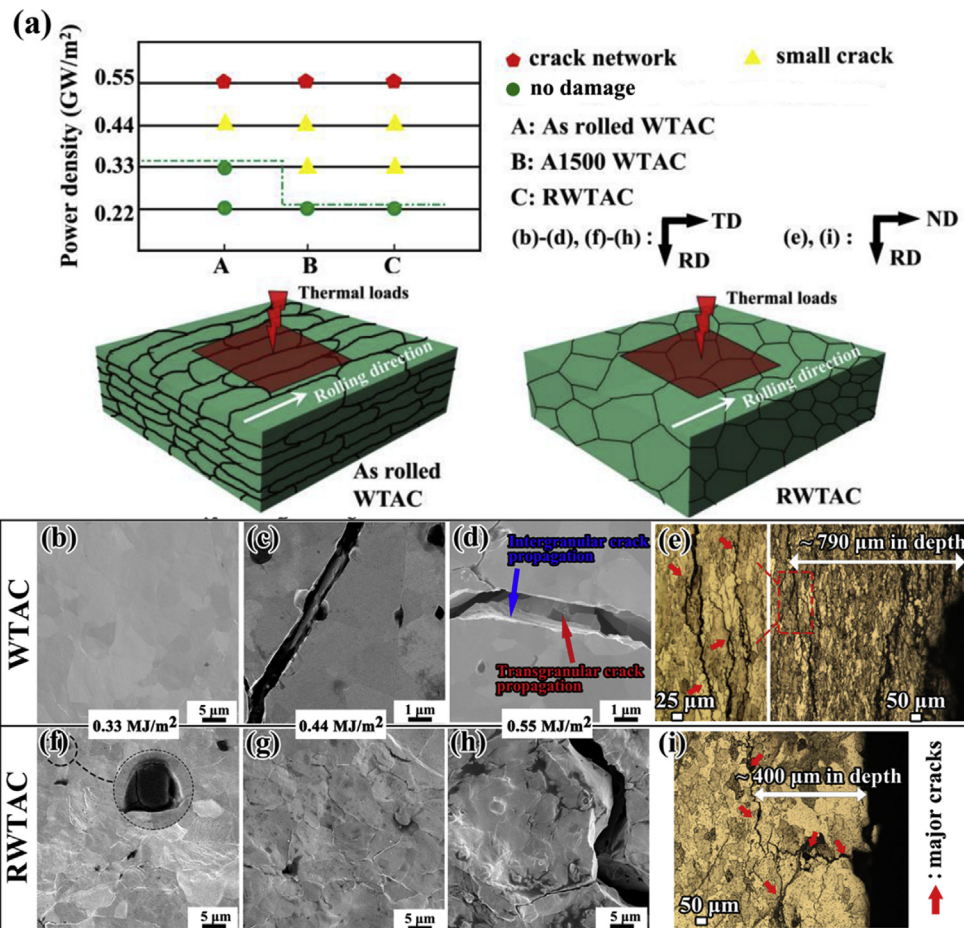


Fig. 8. Thermal shock response of WTAC and RWTAC: (a) An overview of thermal shock response after 100 thermal shock events at different APD, (b–d) SEM images showing the thermal loaded surfaces of WTAC at different APDs, (e) optical micrograph of cross section for WTAC samples at APD ~0.55 GW/m², (f–h) SEM images showing the thermal loaded surfaces of RWTAC at different APDs and (i) optical micrograph of cross section for RWTAC samples at APD ~0.55 GW/m².

small cracks on the loaded area (see Fig. 8f) appeared under an APD of 0.33 GW/m^2 . A large amount of micro-cracks within the loaded area at 0.44 GW/m^2 (see Fig. 8g) were detected and obvious crack networks were formed at 0.55 GW/m^2 . Crack networks, formed at 0.55 GW/m^2 , were generated by predominant intergranular cracks along the grain boundaries as can be seen in Fig. 8h and i, which indicated that recrystallization may cause degradation of thermal shock resistance. The cracking depth is about $400 \mu\text{m}$ for the

RWTAC after 100 shots with the APD of 0.55 GW/m^2 as shown in Fig. 8i. That's to say, after 100 thermal shots with the APD of 0.55 GW/m^2 , cracks (crack networks) with the larger density but lower cracking depth were observed in the RWTAC compared to that of the WTAC.

In order to explore the crack formation and propagation mechanisms, more detailed microstructure analyses have been conducted. Significant black pittings were observed in damaged

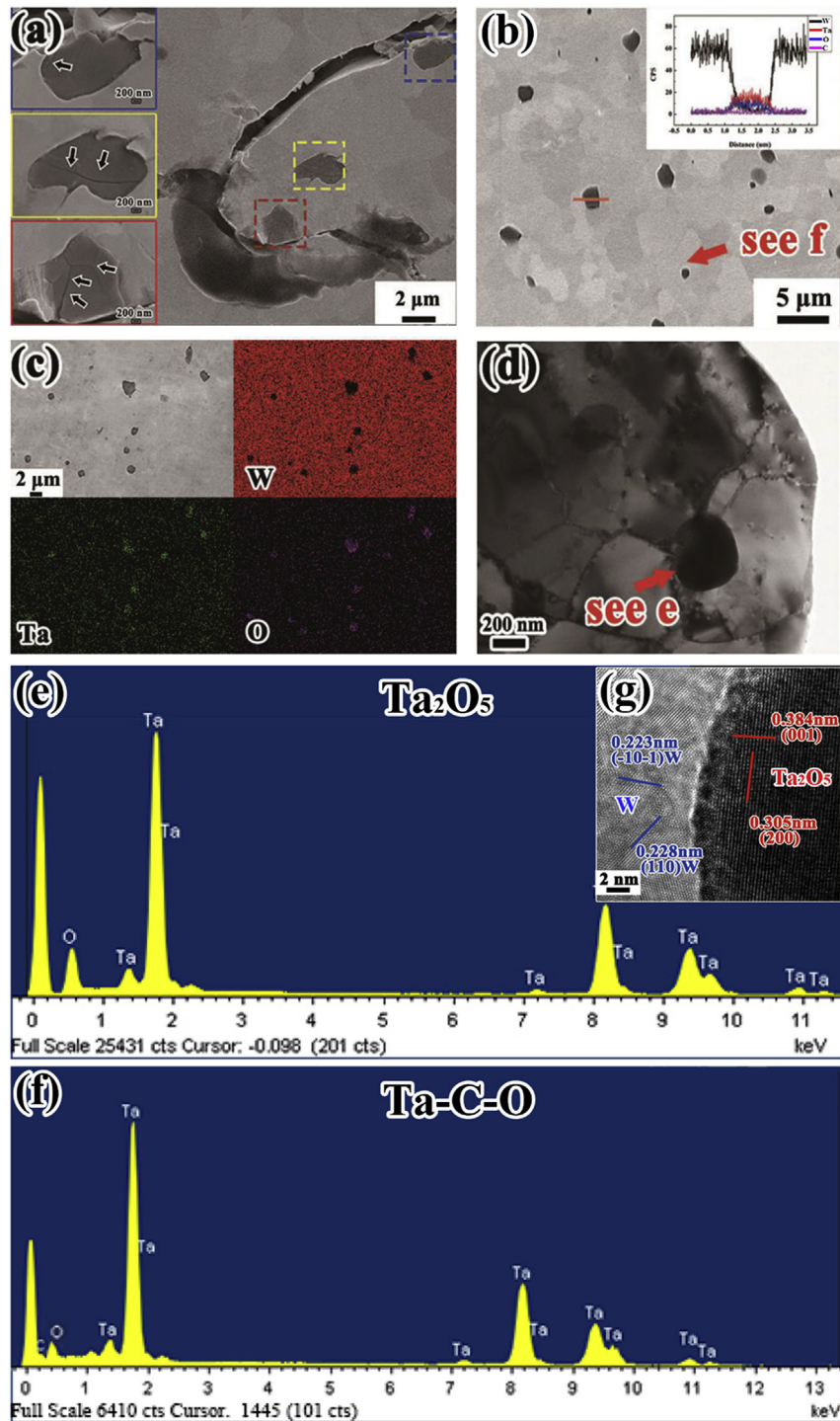


Fig. 9. The characterization of loaded surfaces after 100 pulses thermal shock tests of WTAC at 0.55 GW/m^2 (a) nano cracks in the black pitting, (b) EDS line-scan for the pitting area, (c) EDS mapping, (d) TEM micrograph of coarse particles located at GBs, (e) the TEM-EDS result for the particle, (f) the EDS result for the pointed particle and (g) the measured spaces of orthorhombic Ta_2O_5 particle.

surfaces under the APD conditions ranging from 0.44 to 0.55 GW/m² for both samples. Nano cracks (~30 nm in width) were observed inside these pitting areas on the surface of WTAC as shown in Fig. 9a and insets. The detailed information of pitting areas were investigated by EDS line-scan (Fig. 9b) and mapping (Fig. 9c). Fig. 9b and c shows the corresponding EDS results: the coexistence of Ta and O signals in pitting areas is obviously detected, implying concentrated Ta_xO_y compositions or particles in these areas. To further clarify the phase of such coarse particles, a spherical particle located at a triple GB (see Fig. 9d) was analyzed through the HRTEM in the WTAC sample. The measured spaces of two different crystalline faces (001) and (200) are 0.384 nm and 0.305 nm, respectively, as shown in Fig. 9g. These measured crystalline faces of (001) and (200) match well to the orthorhombic Ta₂O₅ phase crystalline parameters from the powder diffraction file card (reference code: 00-008-0255). The EDS (Fig. 9e) and crystalline faces (Fig. 9g) results indicated that these coarse particles are Ta₂O₅. The formation of Ta₂O₅ particles is most probably attributed to TaC capturing impurity oxygen during sintering, because the powder metallurgy fabrication inevitably introduces impurity oxygen [16,44]. Ta₂O₅ particle formation may result from high oxygen concentration within powders. Actually, Ta-C_xO_y compounds (see Fig. 9f) also existed in the area where the oxygen concentration may be moderate or low. The low thermal conductivity and low melting point of Ta₂O₅ (~4 W/m·K, 1870 °C) particles involved the risk of overheating/melting during thermal shock tests and enhanced erosion of surface area as shown in Figs. 8f and 9a. These weak coarse Ta₂O₅ (or Ta-C_xO_y) particles were prone to decohesion and fracture during cyclic heat loads, which resulted in nano cracks initiating around or in the Ta₂O₅ (or Ta-C_xO_y) particles and then evolving into transgranular cracks in WTAC samples as shown in Fig. 10a–d. Based on the above analysis of the cracking patterns in the WTAC, it could be concluded that transgranular cracks started at the weak interfaces between the Ta₂O₅ or Ta-C_xO_y particles and the tungsten matrix, and then extended parallel to the load surface or into the depth along the GBs as shown in the schematic Fig. 10e. However, in the RWTAC cracks initiated at GBs and then grown along the GBs as shown in Fig. 10f and g, owing to the low cohesion of GBs in the recrystallization stage. On the cross sections for RWTAC, predominantly intergranular cracks were observed (see Fig. 10h), which indicated that grain growth became a major negative effect on thermal shock resistance of RWTAC. That's to say, for the RWTAC, the crack initiation occurrence was mainly attributed to the poor

cohesion of recrystallized grains and crack propagation was also predominantly along the GBs as shown in the schematic Fig. 10i. Overall, doping nanosized particles into W matrix could pin dislocations, refine grains, improve mechanical properties and enhance thermal shock resistances. On the other hand, coarse Ta₂O₅ (or Ta-C_xO_y) particles may introduce the crack initiation during cyclic heat loads.

4. Conclusion

In this work, the tantalum carbide dispersion strengthened W-1.0 wt% TaC alloy was fabricated. Recrystallization behaviors of the rolled WTAC have been investigated using conventional heat treatments with isochronal experiments, which indicate the recrystallization temperature of the WTAC alloys is 1400 °C. The observed recrystallization activation energy is ~478 kJ/mol. The recrystallization temperature and recrystallization activation energy of the WTAC are higher than that of the similarly deformed pure W (~1200 °C, 357 kJ/mol) [33]. The DBTTs of the WTAC and RWTAC are all about 200 °C which are equal to the recently reported rolled pure W [35], swaged W-0.5HfC (WHfC) alloy [36], and about 100 °C higher than that of the rolled W-0.5ZrC (WZrC) alloy [24]. The UTS of the WTAC is similar to the swaged WHfC, slightly lower than that of the WZrC and about 200 MPa higher than that of the rolled pure W. Nanosized particles located at GBs could hinder GB migration, reduce grain growth and thus refine grains, which could improve the strength but to some extent decrease the tensile elongation of the W-1.0 wt% TaC alloy.

The effect of transient thermal loads (100 shots at RT) on the as-rolled and fully recrystallized W-1.0 wt% TaC alloys have been investigated by employing an electron beam test facility. The cracking thresholds are in the range of 0.22–0.33 GW/m² for RWTAC and 0.33–0.44 GW/m² for the WTAC, respectively, at RT with 100 shots. These cracking thresholds are slightly larger than that of the forged (and recrystallized) W-UHP (~0.2 GW/m² at RT) [21]. The thermal shock induced cracks are related to the microstructures like second phase particles and GBs: coarse Ta₂O₅ and Ta-C_xO_y particles in WTAC and weak GBs from the recrystallization and grain growth in RWTAC becoming preferential crack initiations. However, more experiments for the disruption-like and ELM-like tests are needed to confirm the thermal shock resistance and identify the reliabilities for application in reactor conditions.

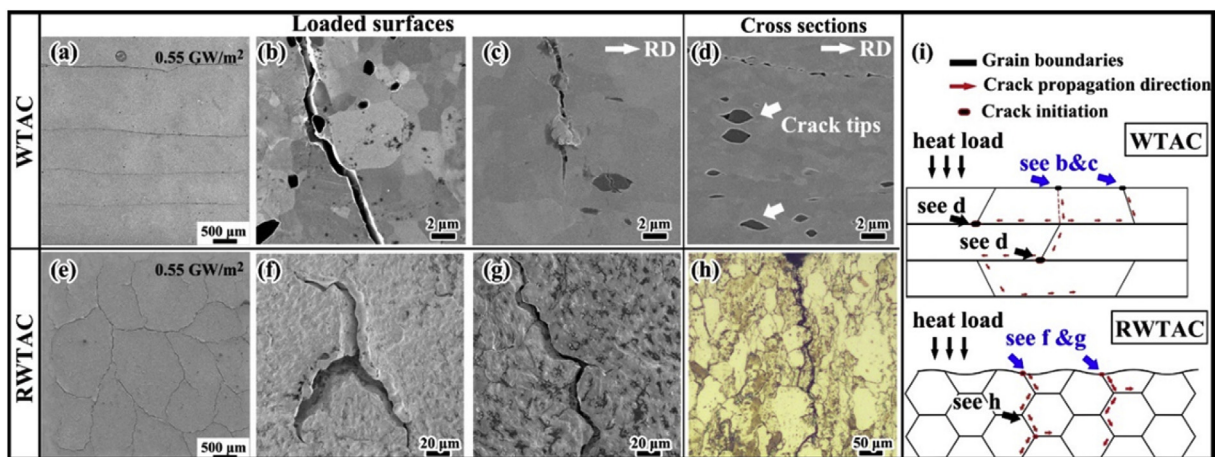


Fig. 10. SEM and schematic images illustrating the crack formation mechanism in WTAC and RWTAC samples. (a) cracks on WTAC samples at 0.55 GW/m², (b) transgranular cracks in WTAC, (c, d) transgranular cracks through or near coarse particles in WTAC, (e) cracks on RWTAC samples at 0.55 GW/m², (f–h) cracks along the grain boundaries and (i) sketches showing the crack formation in WTAC and RWTAC, respectively.

Acknowledgements

This work was financial supported by the National Key Research and Development Program (2017YFA0402800) and the National Natural Science Foundation of China (with Grant Nos.11575241, 11735015, 11575231, 11735230, 11475216, 51671184 and 11405203).

References

- [1] V. Philipps, J. Nucl. Mater. 415 (2011) S2–S9.
- [2] J. Knaster, A. Moeslang, T. Muroga, Nat. Phys. 12 (2016) 424–434.
- [3] M. Rieth, S.L. Dudarev, S.M.G. De Vicente, J. Aktaa, T. Ahlgren, S. Autusch, D.E.J. Armstrong, M. Balden, N. Baluc, M. Barthe, J. Nucl. Mater. 432 (2013) 482–500.
- [4] I. Uytendhouwen, T. Schwarzslinger, J.W. Coenen, M. Wirtz, Phys. Scripta 2016 (2016) 014007.
- [5] J.S.K.L. Gibson, S.G. Roberts, D.E.J. Armstrong, Mater. Sci. Eng. A 625 (2015) 380–384.
- [6] A. Giannattasio, Z. Yao, E. Tarleton, S.G. Roberts, Philos. Mag. A 90 (2010) 3947–3959.
- [7] G. Pintsuk, 4.17-Tungsten as a plasma-facing material A2-Konings, in: J.M. Rudy (Ed.), Comprehensive Nuclear Materials, Elsevier, Oxford, 2012, pp. 551–581.
- [8] M. Li, E. Werner, J.-H. You, Fusion Eng. Des. 89 (2014) 2716–2725.
- [9] A. Alfonso, D. Juul Jensen, G.N. Luo, W. Pantleon, J. Nucl. Mater. 455 (2014) 591–594.
- [10] K. Farrell, A. Schaffhauser, J. Stiegler, J. Less Common Met. 13 (1967) 141–155.
- [11] A. Babak, E. Uskov, Strength Mater. 15 (1983) 667–672.
- [12] W.-S. Lee, C.-F. Lin, G.-L. Xie, Mater. Sci. Eng. A 247 (1998) 102–112.
- [13] S. Wurster, N. Baluc, M. Battabyal, T. Crosby, J. Du, C. García-Rosales, A. Hasegawa, A. Hoffmann, A. Kimura, H. Kurishita, J. Nucl. Mater. 442 (2013) S181–S189.
- [14] H. Kurishita, S. Matsuo, H. Arakawa, T. Sakamoto, S. Kobayashi, K. Nakai, H. Okano, H. Watanabe, N. Yoshida, Y. Torikai, Phys. Scripta 2014 (2014) 014032.
- [15] R. Liu, Z. Xie, T. Zhang, Q. Fang, X. Wang, T. Hao, C. Liu, Y. Dai, Mater. Sci. Eng. A 660 (2016) 19–23.
- [16] S. Miao, Z. Xie, X. Yang, R. Liu, R. Gao, T. Zhang, X. Wang, Q. Fang, C. Liu, G. Luo, Int. J. Refract. Metals Hard Mater. 56 (2016) 8–17.
- [17] Y. Ueda, M. Oya, Y. Hamaji, H. Lee, H. Kurishita, Y. Torikai, N. Yoshida, A. Kreter, J. Coenen, A. Litnovsky, Phys. Scripta 2014 (2014) 014038.
- [18] R.A. Pitts, S. Carpentier, F. Escourbiac, T. Hirai, V. Komarov, S. Lisgo, A.S. Kukushkin, A. Loarte, M. Merola, A. Sashala Naik, R. Mitteau, M. Sugihara, B. Bazylev, P.C. Stangeby, J. Nucl. Mater. 438 (2013) S48–S56.
- [19] A. Loarte, G. Saibene, R. Sartori, V. Riccardo, P. Andrew, J. Paley, W. Fundamenski, T. Eich, A. Herrmann, G. Pautasso, A. Kirk, G. Counsell, G. Federici, G. Strohmayr, D. Whyte, A. Leonard, R.A. Pitts, I. Landman, B. Bazylev, S. Pestchanyi, Phys. Scripta T128 (2007) 222–228.
- [20] T. Hirai, S. Panayotis, V. Barabash, C. Amzallag, F. Escourbiac, A. Durocher, M. Merola, J. Linke, T. Loewenhoff, G. Pintsuk, M. Wirtz, I. Uytendhouwen, Nuclear Mater. Energy 9 (2016) 616–622.
- [21] M. Wirtz, G. Cempura, J. Linke, G. Pintsuk, I. Uytendhouwen, Fusion Eng. Des. 88 (2013) 1768–1772.
- [22] M. Wirtz, J. Linke, G. Pintsuk, L. Singheiser, M. Zlobinski, J. Nucl. Mater. 438 (2013) S833–S836.
- [23] T. Hirai, G. Pintsuk, J. Linke, M. Batilliot, J. Nucl. Mater. 390 (2009) 751–754.
- [24] Z.M. Xie, S. Miao, R. Liu, L.F. Zeng, T. Zhang, Q.F. Fang, C.S. Liu, X.P. Wang, Y.Y. Lian, X. Liu, L.H. Cai, J. Nucl. Mater. 496 (2017) 41–53.
- [25] Z.M. Xie, R. Liu, S. Miao, X.D. Yang, T. Zhang, X.P. Wang, Q.F. Fang, C.S. Liu, G.N. Luo, Y.Y. Lian, X. Liu, Sci. Rep. 5 (2015) 16014.
- [26] M. Zhao, Z. Zhou, M. Zhong, J. Tan, Mater. Sci. Eng. A 646 (2015) 19–24.
- [27] G. Pintsuk, H. Kurishita, J. Linke, H. Arakawa, S. Matsuo, T. Sakamoto, S. Kobayashi, K. Nakai, Phys. Scripta T145 (2011) 014060.
- [28] Y. Lian, X. Liu, Z. Xu, J. Song, Y. Yu, Fusion Eng. Des. 88 (2013) 1694–1698.
- [29] X. Zhang, Q. Yan, J. Nucl. Mater. 444 (2014) 428–434.
- [30] O.M. Wirtz, Thermal shock Behaviour of Different Tungsten Grades under Varying Conditions, vol. 161, Forschungszentrum Jülich, 2012. <http://hdl.handle.net/2128/5136>.
- [31] M. Wirtz, I. Uytendhouwen, V. Barabash, F. Escourbiac, T. Hirai, J. Linke, Th. Loewenhoff, S. Panayotis, G. Pintsuk, Nucl. Fusion 57 (2017) 066018.
- [32] G. Pintsuk, S. Antusch, T. Weingaertner, M. Wirtz, Int. J. Refract. Metals Hard Mater. 72 (2018) 97–103.
- [33] A. Alfonso, D. Juul Jensen, G.N. Luo, W. Pantleon, Fusion Eng. Des. 98–99 (2015) 1924–1928.
- [34] F.J. Humphreys, M. Hatherly, Chapter 5-The Mobility and Migration of Boundaries, Recrystallization and Related Annealing Phenomena, second ed., Elsevier, Oxford, 2004, pp. 121–129.
- [35] T. Shen, Y. Dai, Y. Lee, J. Nucl. Mater. 468 (2016) 348–354.
- [36] Y.K. Wang, S. Miao, Z.M. Xie, R. Liu, T. Zhang, Q.F. Fang, T. Hao, X.P. Wang, C.S. Liu, X. Liu, L.H. Cai, J. Nucl. Mater. 492 (2017) 260–268.
- [37] L. Erik, S. Wolf-Dieter, New York. Plenum Publishers, 1999.
- [38] W. Martienssen, H. Warlimont, Springer handbook of Condensed Matter and Materials Data, Springer Science & Business Media, 2006.
- [39] J. Neges, B. Ortner, G. Leichtfried, H.P. Stüwe, Mater. Sci. Eng. A 196 (1995) 129–133.
- [40] H. Kurishita, Y. Kitsunai, T. Shibayama, H. Kayano, Y. Hiraoka, J. Nucl. Mater. 233–237 (1996) 557–564.
- [41] M. Wirtz, J. Linke, T. Loewenhoff, G. Pintsuk, I. Uytendhouwen, Phys. Scr., T 167 (2016) 014015.
- [42] M. Wirtz, A. Kreter, J. Linke, Th. Loewenhoff, G. Pintsuk, G. Sergienko, I. Steudel, B. Unterberg, E. Wessel, Phys. Scr., T 170 (2017) 014066.
- [43] J. Linke, T. Loewenhoff, V. Massaut, G. Pintsuk, G. Ritz, M. Rödig, A. Schmidt, C. Thomser, I. Uytendhouwen, V. Vasechko, M. Wirtz, Nucl. Fusion 51 (2011) 073017.
- [44] T. Jun, Z.-J. Zhou, X.-P. Zhu, S.-Q. Guo, D.-D. Qu, M.-K. Lei, C.-C. Ge, Trans. Nonferrous Metals Soc. China 22 (2012) 1081–1085.